

**Bayes-Turchin analysis of x-ray absorption data above the Fe  $L_{2,3}$ -edges**H. H. Rossner, D. Schmitz, P. Imperia, and H. J. Krappe  
*Hahn-Meitner-Institut Berlin, Glienicker Strasse 100, D-14109 Berlin, Germany*

J. J. Rehr

*Department of Physics, University of Washington, Seattle, Washington 98195-1560, USA*

(Received 23 May 2006; revised manuscript received 12 August 2006; published 13 October 2006)

Extended x-ray absorption fine structure (EXAFS) data and magnetic EXAFS (MEXAFS) data were measured at two temperatures (180 and 296 K) in the energy region of the overlapping  $L$ -edges of bcc Fe grown on a V(110) crystal surface. In combination with a Bayes-Turchin data analysis procedure these measurements enable the exploration of local crystallographic and magnetic structures. The analysis determined the atomic-like background together with the EXAFS parameters which consisted of ten shell radii, the Debye-Waller parameters, separated into structural and vibrational components, and the third cumulant of the first scattering path. The vibrational components for 97 different scattering paths were determined by a two parameter force-field model using *a priori* values adjusted to Born-von Karman parameters of inelastic neutron scattering data. The investigations of the system Fe/V(110) demonstrate that the simultaneous fitting of atomic background parameters and EXAFS parameters can be performed reliably. Using the  $L_2$ - and  $L_3$ -components extracted from the EXAFS analysis and the rigid-band model, the MEXAFS oscillations can only be described when the sign of the exchange energy is changed compared to the predictions of the Hedin Lundquist exchange and correlation functional.

DOI: [10.1103/PhysRevB.74.134107](https://doi.org/10.1103/PhysRevB.74.134107)

PACS number(s): 61.10.Ht, 78.20.Ls, 78.70.Dm, 87.64.Fb

**I. INTRODUCTION**

Extended x-ray absorption fine structure (EXAFS) oscillations represent a unique signal of the local atomic structure and of the vibrational properties of matter. Being element specific and applicable in periodic as well as in aperiodic materials with spatial resolution of roughly 2 pm, EXAFS is a very important probe in material science.<sup>1</sup> Use of a high flux circular polarized photon source with variable energy provides the possibility of adding magnetic selectivity to the scope of EXAFS. This achievement is of particular importance in the soft x-ray regime for magnetic studies at the  $L$ -edges of  $3d$ -transition metals, where the knowledge of magnetic short-range order, i.e., the magnetic spin moments of neighboring atoms and the exchange-correlation potential of electron-electron scattering, is essential for the physical understanding of ferromagnetism. For the investigation of the spin dependence of this potential we use the rigid-band model and the relation it provides between EXAFS and magnetic EXAFS (MEXAFS) oscillations. This model can be tested if a reliable EXAFS data analysis for overlapping  $L$ -edges is available.

In the soft x-ray regime the analysis of EXAFS data faces substantial difficulties due to the small spin-orbit splitting of the  $2p$  states. Previously partly overlapping  $L_3$ -,  $L_2$ -, and  $L_1$ -edge EXAFS spectra were simultaneously analyzed using the multiple-edge data-analysis based on the  $n$ -body distribution functions  $g_n$  in x-ray absorption spectroscopy (GNXAS method).<sup>2</sup> It has been shown that multiple-edge studies are able to increase accuracy and consistency of the short-range structural results. In contrast to our analysis procedure<sup>3</sup> the extended GNXAS method did not explicitly include the atomiclike background contribution in the fitting procedure and thus neglects the error correlations between background parameters and structural parameters. In the usual EXAFS

analysis the structural oscillation is extracted from the absorption data by subtraction of a background function modelled by a smooth polynomial spline. This method is questionable when background anomalies due to multiple-electron excitation,<sup>4</sup> atomic EXAFS,<sup>5,6</sup> or systematic experimental errors<sup>7</sup> are present. The difficulties in analyzing overlapping  $L$ -edges and background anomalies are solved by our Bayes-Turchin data-analysis procedure.<sup>3,7</sup> In this procedure the uncertainties of experimental data and model parameters are taken into account, and the measured absorption data are normalized to results of the FEFF8.2 code.<sup>8</sup>

The EXAFS Debye-Waller (DW) parameters are composed of structural and vibrational disorder in bond distances, and a force-field model is used for the description of the vibrational component starting with parameters extracted from inelastic neutron scattering data. A slight modification of the recursion method suggested by Poiarkova and Rehr<sup>9,10</sup> to construct the projected vibrational density of states (VDOS) enables the description of the local unprojected VDOS and thus the comparison with inelastic neutron scattering results. This comparison relates the local phonon state density of a finite cluster to the global phonon state density of an infinite lattice.

The existence of x-ray magnetic circular dichroism (XMCD) was first demonstrated for the  $K$ -edge of ferromagnetic iron<sup>11</sup> in the near edge region, and these measurements also indicated a dichroic contribution in the EXAFS region. In the edge region the XMCD signal is caused by the filling of states with different magnetic quantum numbers  $m_l$ , whereas in the extended energy region, where all  $m_l$  states are unoccupied and equally available for transitions, the dichroic signal is due to the spin-orbit splitting and the exchange correlation potential of the photoelectron.<sup>12,14</sup> Within a rigid-band model magnetic EXAFS can be described by the difference of two EXAFS spectra shifted by an exchange-

related energy.<sup>6,15</sup> This suggests that XMCD measurements in the extended energy region provide a significant test of excited state exchange-correlation potentials. Using an approximate theory of XMCD, investigations of various exchange models were performed at the  $L_2$  and  $L_3$  edges of Gd with half-filled core levels.<sup>12,13</sup> It turned out that sign, amplitude and general form of the XMCD signal agreed reasonably well with experiment. Ebert *et al.*<sup>16</sup> applied a fully relativistic description of MEXAFS to data of the  $L_{2,3}$ -edges of bcc-Fe taken at the second generation synchrotron BESSYI. In this analysis a discrepancy was noted between theoretical and experimental spectra. Most of the discrepancy could be removed by self-energy corrections to the excitation energy, but this analysis clearly demonstrated the need for better experimental data. Using the third generation synchrotron BESSYII the quality of the measured data and thus the investigation of the self energy could be improved.

The experimental details are described in Sec. II. In Sec. III we present our Bayes-Turchin data-analysis procedure for overlapping  $L$ -edges with simultaneous determination of the atomiclike background. In this section we further describe the treatment of lattice dynamics, sketch the relation between EXAFS and MEXAFS oscillations, and discuss the results. Conclusions are given in Sec. IV. The “penalty” probability used to determine the background function is described in Appendix A. A recursion relation for the calculation of the unprojected VDOS for a finite cluster of atoms and corrections to suppress contributions of spurious rigid motions of the cluster to the VDOS are given in Appendix B.

## II. EXPERIMENTAL SETUP

To get an epitaxial Fe film with the fewest amount of impurities the sample material was prepared under UHV conditions at a base pressure of  $5 \times 10^{-10}$  mbar in the experimental chamber. The surface of the V(110) crystal had been cleaned by sputtering and annealing cycles using  $\text{Ar}^+$  ions with kinetic energy of 700 eV and a maximum annealing temperature of 800 °C. Performing electron beam evaporation from a pure iron rod a film of thickness  $\approx 60$  Å was deposited with a rate of about 0.3 Å/min. It has been assumed that effects of the interface of the Fe/V(110) system can be neglected at this film thickness. Usually magnetic materials exhibit a high surface free energy compared to non-magnetic metal materials. The surface free energy of Fe-bcc(110) is  $\sigma_{\text{Fe}} = 3.09 \text{ J m}^{-2}$  and the surface free energy of V-bcc(110) is  $\sigma_{\text{V}} = 2.02 \text{ J m}^{-2}$ ,<sup>17</sup> which may yield an unfavorable wetting of the V surface. The crystal lattice misfit  $f = (a_{\text{Fe}} - a_{\text{V}})/a_{\text{Fe}}$  between V-bcc with  $a = 3.024$  Å (Ref. 18) and Fe-bcc with  $a = 2.8665$  Å (Ref. 18) is small,  $f = -0.055$ , and should favor good grow conditions. It has been shown, that these conditions finally result in epitaxial Fe films with an easy axis of the magnetization direction parallel to the film plane,<sup>19–21</sup> and that the bulk magnetic moment of  $2.2\mu_B$  is reached at and above 5 monolayers of Fe thickness  $t_{\text{Fe}}$  (Ref. 21) corresponding to  $t_{\text{Fe}} \approx 7$  Å.

The measurements have been performed at the elliptical undulator beamline UE46-PGM at BESSY (Ref. 22) using the fifth harmonic of circularly polarized light, the

1200 l/mm blazed grating and an exit slit of 100  $\mu\text{m}$ , resulting in an energy resolution of  $\Delta E/E \approx 0.1\%$ . To preserve brightness and a circular photon polarization  $P_c = 0.9$  of the incoming beam over the whole EXAFS energy region, the undulator gap scan technique<sup>23</sup> was used. This procedure interpolates the optimum values for gap size and row shift from tabulated values and adjusts the undulator setting at each monochromator energy step. The tabulated values for gap size and row shift had been set up for the fifth harmonic peak position in the energy range of 700–1700 eV with step size of 50 eV.

The (M)EXAFS measurements were carried out in remanence recording the total electron yield of the sample and the drain current of the last beamline mirror within the energy range of 690–1160 eV. X rays with positive helicity were used and the magnetization direction of the sample was switched relative to the beam direction at each energy step. The data were taken at two temperatures of 180 and 296 K, measured by a thermocouple positioned close to the sample. Using sample transfer in UHV conditions usually results in an indirect measurement of the sample temperature and often suffers from weak thermal contacts between sample and thermocouple. We estimate the uncertainty of the sample temperature at  $T = 180$  K to  $\pm 5$  K and at  $T = 296$  K to  $\pm 1$  K. A pulsed external field of 350 Oe has been applied to magnetize the Fe film along its easy axis parallel to the surface plane. The angle between the incoming beam direction and the surface plane was 20°. At each energy point the absorption coefficients  $\mu^+$  and  $\mu^-$ , that correspond to parallel and antiparallel orientation of the photon helicity with respect to the magnetization vector, were measured twice flipping the direction of the external magnetic field alternately. The unnormalized spin-averaged absorption coefficient is obtained by  $\mu'(E) = [\mu^+(E) + \mu^-(E)]/2$  and the corresponding magnetic signal by  $\mu^{M'}(E) = \mu^+(E) - \mu^-(E)$ . Minimal correction factors of  $f_{\text{corr}} = 1 \pm 0.0002$  for  $\mu^\pm$  were needed to bring the offset of  $\mu^{M'}(E)$  to zero at the high energy tail. We note that the systematic error of the MEXAFS signal is reduced considerably at this beamline when the magnetization direction of the sample is switched at each energy step instead of the photon beam helicity. The  $L_{2,3}$ -edge regions of the experimental data  $\mu'$  and  $\mu^{M'}$  are shown in Fig. 1. The “296 K” line represents the first scan of the experiment and the “180 K” line displays the last scan. No significant differences in the spectral shapes are observed, indicating that no significant oxidation of the Fe film occurred. The magnetic signals have been rescaled for full circular photon polarization  $P_c = 1$  and for complete alignment of the sample magnetization along the photon beam direction. At each temperature the data of four scans were added to improve statistics, and the pre-edge background of  $\mu'$ , described by a straight line, was adjusted to the pre-edge region and subtracted from  $\mu'$ .

## III. DATA ANALYSIS AND DISCUSSION

### A. EXAFS spectra

For the EXAFS analysis of overlapping  $L$ -edges we follow the procedure suggested in Ref. 3. The reference energy

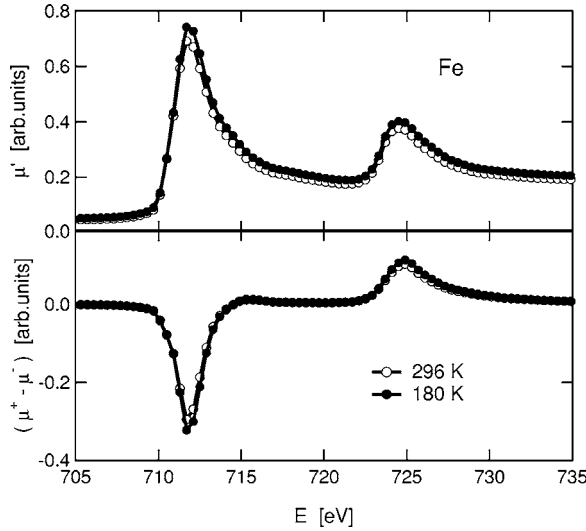


FIG. 1. Spin-averaged absorption coefficient  $\mu'$  and dichroic signal  $\mu^{M'}$  measured in the near-edge region at temperatures of 296 and 180 K.

$E_0 = E_{0,L_3}$  refers to the  $L_3$  edge and defines the wave vector  $k = \sqrt{2m(E - E_0)}/\hbar$ . To express the EXAFS spectra of the  $L_1$  and  $L_2$  edges in terms of  $k$ , shifted wave vectors  $k_s$  are introduced

$$k_s^2(k) = k^2 - 2m[E_{0,L_s} - E_0]/\hbar^2, \quad s = 1, 2. \quad (1)$$

The normalized atomiclike background-absorption coefficients  $\mu_{0,L_s}(k_s)$  of the FEFF code, given in units of  $\text{\AA}^2$ , are smoothed and written as  $\overline{\mu_{0,L_s}(k)}$ . The  $k$ -dependent relative strengths of these coefficients for edges  $L_1$  and  $L_2$  are called  $\alpha_s(k)$

$$\alpha_s(k) = \frac{\overline{\mu_{0,L_s}(k)}}{\sum_{i=1}^3 \overline{\mu_{0,L_i}(k)}}, \quad s = 1, 2. \quad (2)$$

These  $\alpha_s(k)$  values are used to extract a smooth  $L_3$  component  $\overline{\mu'_{L_3}(k)}$  from the measured data  $\mu'(k)$ :

$$\overline{\mu'_{L_3}(k)} = \overline{\mu(k)[1 - \alpha_1(k) - \alpha_2(k)]}, \quad (3)$$

and to construct the smooth detector efficiency  $A(k)$

$$A(k) = \frac{\overline{\mu'_{L_3}(k)}}{\overline{\mu_{0,L_3}(k)}}. \quad (4)$$

The factor  $A(k)^{-1}$  is applied to normalize the measured absorption coefficient to FEFF results, expressed in units of  $\text{\AA}^2$ . The FEFF calculations were performed using the complex-energy dependent Hedin-Lundqvist (HL) exchange-correlation potential.<sup>24</sup> The normalization takes into account systematic experimental uncertainties of low frequencies such as post-edge saturation effects<sup>25</sup> and differences in the energy dependence of sample drain current and mirror drain current. It is emphasized that this post-edge normalization function cannot be applied in the edge and pre-edge energy

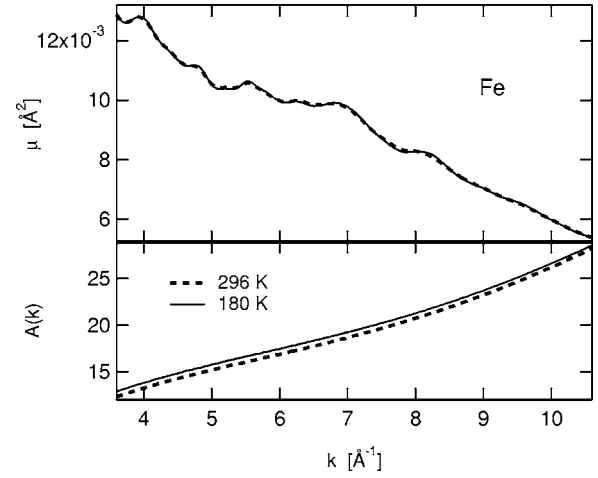


FIG. 2. Normalized data  $\mu(k)$  (upper panel) and detector efficiency  $A(k)$  (lower panel) at temperatures of 296 K (dashed line) and 180 K (solid line).

regions due to very different absorption coefficients in these regions. In the following we will use the normalized experimental data  $\mu(k) = \mu'(k)/A(k)$  and  $\mu^M(k) = \mu^{M'}(k)/A(k)$ . The normalized data  $\mu(k)$  and the detector efficiency  $A(k)$  are displayed in Fig. 2 for the two temperatures of 296 K (dashed line) and 180 K (solid line). The overlapping curves of  $\mu(k)$  in the upper panel demonstrate that low frequency systematic errors of measurement and pre-edge background subtraction are corrected by  $A(k)$  (lower panel).

To compare the experimental data with model parameters we consider the following expressions of the multiple path expansion:

$$\mu(k) = \sum_{s=1}^3 [\mu_{0,L_s}(k) + \delta\mu_{0,L_s}(k)][\chi_{L_s}(k) + 1], \quad (5)$$

$$\chi_{L_s}(k) = \frac{S_{0,L_s}^2}{k} \sum_j N_j \frac{|f_{j,L_s}(k, R_j)|}{R_j^2} e^{-2k^2\sigma_j^2 - 2R_j/\lambda_{L_s}(k)} \times \sin(k, R_j, \phi_{j,L_s}, C_{3,j}), \quad (6)$$

$$\sin(k, R_j, \phi_{j,L_s}, C_{3,j}) = \sin \left[ 2k[R_j - \delta R_{j,L_s}(k)] + \phi_{j,L_s}(k) - \frac{4}{3}C_{3,j}k^3 \right], \quad (7)$$

$$\delta R_{j,L_s}(k) = 2\sigma_j^2[R_j^{-1} + \lambda_{L_s}(k)^{-1}] + \delta R_{j,\perp}. \quad (8)$$

The EXAFS functions  $\chi_{L_s}(k)$  are written for each edge  $L_s$  in terms of the overall amplitude correction factors  $S_{0,L_s}^2$ , the edge energies  $E_{0,L_s}$ , the half path lengths  $R_j$  of each unique scattering path  $j$  of degeneracy  $N_j$ , the Debye-Waller parameters  $\sigma_j^2$ , the third cumulants  $C_{3,j}$ , and the energy-dependent effective mean free paths  $\lambda_{L_s}(k)$  which include the core-hole lifetimes of the  $2s$  and  $2p$  states. The first term in the sum of  $\delta R_{j,L_s}(k)$  is customarily used and expresses the difference

between the real and effective first cumulants that correspond to the real and effective average values of the radial distribution. It has been pointed out by Fornasini *et al.*<sup>26</sup> that disorder perpendicular to the scattering path also affects the average distance measured by EXAFS. This is taken into account by the second term  $\delta R_{j,\perp}$  in the argument of the sin function using the approximation

$$\delta R_{j,\perp} = \frac{1}{2} \sum_{i=1}^{N_{at,j}} \frac{\sigma_i^2}{|r_{i-1,i}|}, \quad (9)$$

where  $N_{at,j}$  is the number of atoms of scattering path  $j$ ,  $|r_{i-1,i}|$  is the distance between neighboring atoms  $i$  and  $i-1$ , and  $\sigma_i^2$  is the total DW parameter of path section  $i$ , assuming that the structural and vibrational components are isotropic. Because this second correction term of the effective first cumulant usually is rather small, the thermal vibrations of this term were calculated by the correlated Debye model for each path section, whereas the other thermal vibrations of the above EXAFS formula were calculated by a force-field model. Use of the correlated Debye model implies isotropic vibrations  $2\sigma_{\parallel}^2 = \sigma_{\perp}^2$ . This is only a rough approximation for an otherwise rather small correction term. In Ref. 26 experimental values of  $\sigma_{\perp}^2 / \sigma_{\parallel}^2$  for the first shell of copper were determined and resulted in values larger than 2 and smaller than 3. Considering the first scattering path in Fe with  $R_1 = 2.470 \text{ \AA}$  at  $T = 295 \text{ K}$ , for example, the cumulant correction yields  $0.011 \text{ \AA}$  and the correction term due to perpendicular vibrations yields  $0.002 \text{ \AA}$ .

To allow deviations of the atomlike background functions from FEFF predictions, the correction functions  $\delta\mu_{0,L_s}(k)$  are introduced and described by cubic spline functions at support points  $k_p$ .<sup>3</sup> One may want to determine  $\delta\mu_0$  such that it does not change the dipole sum, which means  $\int_0^{\infty} \delta\mu_0(k) k dk = 0$ . Since  $\delta\mu_0$  is only determined between  $k_1$  and  $k_p$  one may consider the even more stringent condition

$$\int_{k_1}^{k_p} \delta\mu_0(k) k dk = 0. \quad (10)$$

This constraint can be introduced in the fitting procedure by a penalty probability as defined in Appendix A. It turned out that the constraint actually does not affect the fit since  $\delta\mu_0$  automatically fulfills the above condition surprisingly even for rather short  $k$  intervals.

For practical reasons the number of model parameters is reduced in the fit by the following assumptions. (a) Just one correction function  $\delta\mu_0(k_p)$  of  $P=11$  support points on an equally spaced grid is determined and used at all three  $L$ -edges. (b) The reference energy  $E_0$  was set to  $712.6 \text{ eV}$  for both data sets. With this value of  $E_0$  the peak positions of experimental data and model with *a priori* parameters coincide for the EXAFS oscillation at  $k=4 \text{ \AA}^{-1}$ . The energy differences between the  $L_s$  edges were taken from FEFF and were not changed in the fitting process. (c) All three amplitude reduction factors  $S_{0,L_s}^2$  were set to  $S_{0,L_s}^2 = 0.9$ . (d) The first ten single scattering (SS) half-path lengths  $R_j$  were determined starting from perfect bcc-crystal symmetry with crystal parameter  $a=2.8665 \text{ \AA}$ . All multiple scattering (MS) half-path

TABLE I. Fit results using the fixed values  $S_0^2=0.9$  and  $E_0=712.6 \text{ eV}$ . *a priori* and *a posteriori* parameters are shown for the two data sets measured at  $T=180$  and  $296 \text{ K}$ .

$T$ (K)	prior 180,296	post 180	post 296
$\delta\mu_{0,1}$ ( $\text{\AA}^2$ )	0.0	$-4 \times 10^{-5} \pm 4 \times 10^{-5}$	$-3 \times 10^{-5} \pm 4 \times 10^{-5}$
$\delta\mu_{0,2}$ ( $\text{\AA}^2$ )	0.0	$-1 \times 10^{-4} \pm 3 \times 10^{-5}$	$-1 \times 10^{-4} \pm 3 \times 10^{-5}$
$\delta\mu_{0,3}$ ( $\text{\AA}^2$ )	0.0	$+2 \times 10^{-5} \pm 3 \times 10^{-5}$	$+1 \times 10^{-5} \pm 3 \times 10^{-5}$
$\delta\mu_{0,4}$ ( $\text{\AA}^2$ )	0.0	$+9 \times 10^{-5} \pm 3 \times 10^{-5}$	$+1 \times 10^{-4} \pm 3 \times 10^{-5}$
$\delta\mu_{0,5}$ ( $\text{\AA}^2$ )	0.0	$+3 \times 10^{-5} \pm 3 \times 10^{-5}$	$+1 \times 10^{-5} \pm 3 \times 10^{-5}$
$\delta\mu_{0,6}$ ( $\text{\AA}^2$ )	0.0	$-4 \times 10^{-5} \pm 2 \times 10^{-5}$	$-3 \times 10^{-5} \pm 1 \times 10^{-5}$
$\delta\mu_{0,7}$ ( $\text{\AA}^2$ )	0.0	$+2 \times 10^{-5} \pm 1 \times 10^{-5}$	$+1 \times 10^{-5} \pm 1 \times 10^{-5}$
$\delta\mu_{0,8}$ ( $\text{\AA}^2$ )	0.0	$-2 \times 10^{-5} \pm 1 \times 10^{-5}$	$-1 \times 10^{-5} \pm 9 \times 10^{-6}$
$\delta\mu_{0,9}$ ( $\text{\AA}^2$ )	0.0	$+4 \times 10^{-5} \pm 8 \times 10^{-6}$	$+3 \times 10^{-5} \pm 7 \times 10^{-6}$
$\delta\mu_{0,10}$ ( $\text{\AA}^2$ )	0.0	$-3 \times 10^{-5} \pm 6 \times 10^{-6}$	$-2 \times 10^{-5} \pm 6 \times 10^{-6}$
$\delta\mu_{0,11}$ ( $\text{\AA}^2$ )	0.0	$+1 \times 10^{-5} \pm 9 \times 10^{-6}$	$+3 \times 10^{-7} \pm 7 \times 10^{-6}$
$R_1$ ( $\text{\AA}$ )	2.4825	$2.466 \pm 0.008$	$2.470 \pm 0.009$
$R_2$ ( $\text{\AA}$ )	2.8665	$2.845 \pm 0.008$	$2.853 \pm 0.010$
$R_3$ ( $\text{\AA}$ )	4.0538	$4.086 \pm 0.012$	$4.083 \pm 0.014$
$R_4$ ( $\text{\AA}$ )	4.7536	$4.767 \pm 0.013$	$4.768 \pm 0.014$
$R_5$ ( $\text{\AA}$ )	4.9649	$4.970 \pm 0.023$	$4.966 \pm 0.022$
$R_6$ ( $\text{\AA}$ )	5.7330	$5.728 \pm 0.024$	$5.729 \pm 0.023$
$R_7$ ( $\text{\AA}$ )	6.2474	$6.222 \pm 0.023$	$6.233 \pm 0.022$
$R_8$ ( $\text{\AA}$ )	6.4097	$6.421 \pm 0.022$	$6.419 \pm 0.021$
$R_9$ ( $\text{\AA}$ )	7.0215	$7.029 \pm 0.025$	$7.024 \pm 0.023$
$R_{10}$ ( $\text{\AA}$ )	7.4474	$7.450 \pm 0.025$	$7.446 \pm 0.023$
$\kappa_1$ (N/m)	51.688	$51.7 \pm 2.8$	$51.6 \pm 3.0$
$\kappa_2$ (N/m)	16.276	$15.7 \pm 2.8$	$15.2 \pm 2.9$
$\sigma_{\text{struct}}^2$ ( $\text{\AA}^2$ )	0.0	$0.0063 \pm 0.0003$	$0.0072 \pm 0.0003$
$C_{3,1}$ ( $\text{\AA}^3$ )	0.0	$0.0 \pm 2 \times 10^{-5}$	$0.0 \pm 2 \times 10^{-5}$

lengths with  $R_j \leq R_{\text{max}} = 8 \text{ \AA}$  and a relative amplitude of  $A_{\text{rel}} \geq 4\%$  were adjusted properly using the relations between SS and MS paths given in the FEFF data file "paths.dat." (e) As suggested by Sayers *et al.*<sup>27</sup> the total EXAFS DW parameters  $\sigma_j^2$  are separated into independent terms of structural-disorder components  $\sigma_{\text{struct},j}^2$  and thermal-disorder components  $\sigma_{\text{therm},j}^2$ . The thermal components were determined by a force-field model<sup>7,9,10</sup> at  $T=180$  and  $296 \text{ K}$ . The structural-disorder components were assumed to be isotropic and proportional to the number of atoms  $N_{at,j}$  of scattering path  $j$ ,  $\sigma_{\text{struct},j}^2 = \sigma_{\text{struct}}^2 * N_{at,j} / 2$ , where  $\sigma_{\text{struct}}^2$  is the component of a single-scattering path. (f) All third cumulants  $C_{3,j}$  were assumed to be zero except  $C_{3,1}$  which was included in the fit-parameter vector. (g) The  $k$ -dependent effective mean free paths  $\lambda_L(k)$  were taken from FEFF8.2.

The Bayes-Turchin analysis procedure requires as input probability distributions for the experimental data and for the model parameters to account for systematic uncertainties of the model as implemented in FEFF8. The uncertainties of the experimental data points were assumed to be  $0.6\%$  of  $\mu(k)$ . The failure of the multiple-scattering path approach in the edge regions requires the elimination of the data in these regions from the fit. So, very low weights were attributed to

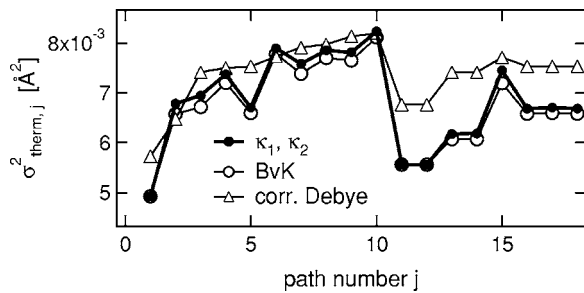


FIG. 3. Thermal DW parameters  $\sigma_{\text{therm},j}^2$  for 18 out of 97 scattering paths calculated at  $T=296$  K. The symbols represent values based on a two-parameter force-field model (solid dots), a 13-parameter force-field model (open circles), and the correlated Debye model (open triangles). Path numbers  $j \leq 10$  correspond to single scattering paths arranged with increasing path lengths. Path numbers above 10 represent DW parameters of multiple scattering paths.

those data points by formally setting the uncertainties to large values ( $10^{13}$ ) inside the regions of  $0 \text{ \AA}^{-1} \leq k \leq 3.6 \text{ \AA}^{-1}$  ( $L_{2,3}$ -edge region) and  $5.9 \text{ \AA}^{-1} \leq k \leq 6.6 \text{ \AA}^{-1}$  ( $L_1$ -edge region). We further assumed L-edge independent model uncertainties for the scattering amplitudes  $f_{j,L_s}(k, R_j)$ , the scattering phases  $\phi_{j,L_s}(k)$ , and the effective mean free paths  $\lambda_{L_s}(k)$  of  $\Delta f_j/f_j=7\%$ ,  $\Delta\phi_j=0.07$  rad, and  $\Delta\lambda/\lambda=15\%$ , respectively. The uncertainties caused by the truncation of the multiple scattering series have been taken into account for each edge separately as explained in Ref. 7 and added quadratically to the other uncertainties of the input.

For the electronic part of the model the conditions  $R_{\text{max}}=8 \text{ \AA}$  and  $A_{\text{rel}} \geq 4\%$  resulted in 97 different scattering paths. For the lattice-vibration part a cluster of 749 atoms arranged in 28 shells within  $R_{\text{max}}=12.8 \text{ \AA}$  was applied to construct the dynamical matrix based on an ideal bcc lattice with crystal parameter  $a$ . A two-parameter force-field model was used with the spring constants  $\kappa_1$  and  $\kappa_2$  corresponding to the nearest neighbor and next-nearest neighbor bond distances. Their *a priori* values (see Table I) were adjusted to EXAFS DW parameters calculated from Born-von Karman (BvK) force constants which had been obtained from inelastic neutron scattering. The phonon dispersion relations of Fe at 295 K had been measured by Minkiewicz *et al.*<sup>28</sup> and analyzed by a BvK model using 13 parameters and five shells. To relate the BvK parameters to the elements of the dynamical matrix, the crystal symmetry of the bcc lattice was taken into account. In Fig. 3 thermal EXAFS DW parameters  $\sigma_{\text{therm},j}^2$  calculated at  $T=296$  K are compared for different models. The first 10 path numbers  $j$  refer to SS paths arranged with increasing path lengths and the higher path numbers represent MS paths. The results of the two-parameter force-field model are represented by solid dots, the results of the 13-parameter force-field model are shown by open circles, and the results of the correlated Debye model with  $\theta_{\text{Debye}}=420$  K are displayed by open triangles. Obviously the DW parameters calculated with 13 BvK force-field parameters can be reproduced very well by the two-parameter force-field model. The one-parameter correlated Debye model values show less path-dependent structure and have

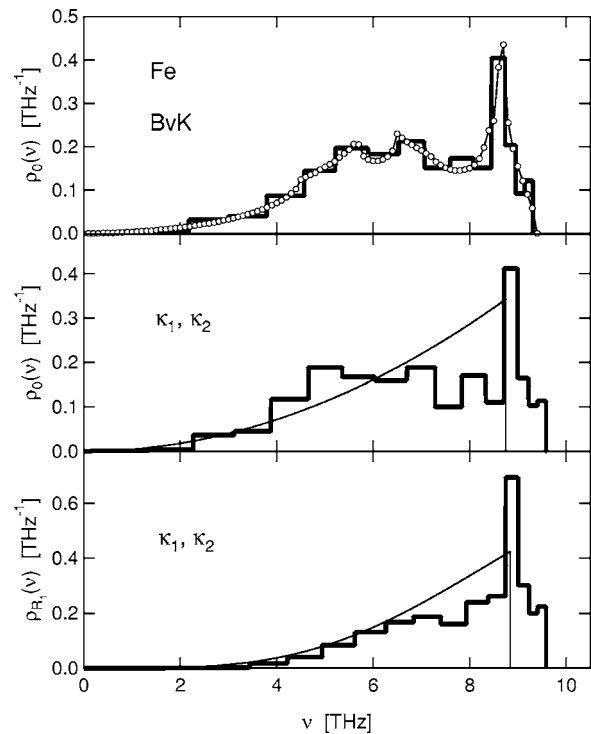


FIG. 4. Comparison of vibrational densities of states. Upper frame: The unprojected VDOS extracted from inelastic neutron scattering is represented by open circles, the calculation based on a force-field model with 13 Born-von Karman model parameters using the recursion method is displayed by the solid line histogram. Middle frame: The unprojected VDOS calculated from a two-parameter force-field model with the *a priori* values of  $\kappa_1$  and  $\kappa_2$  is shown by the histogram. For comparison the Debye model VDOS is included and represented by the thin solid line. Lower frame: The two-parameter force-field model VDOS projected onto the first scattering path is shown by the histogram. The corresponding correlated Debye model VDOS is represented by the thin solid line.

larger values for MS paths. All three models show the "melting" of the EXAFS oscillations with increasing path length.

Thermal DW parameters are defined as a functional of the VDOS.<sup>7</sup> More features of the different models are thus revealed by plots of the corresponding VDOS. Figure 4 compares unprojected and projected state densities. The numerical data of the phonon frequency spectrum extracted from inelastic neutron scattering using the 13-parameter BvK model are tabulated in Ref. 29 and are represented by open circles in the upper frame of Fig. 4. Using the same BvK parameters in the recursion method with order 16 for the calculation of the local VDOS of a finite cluster, we get the results shown by the histogram. This recursion method is based on the algorithm of Poiarkova and Rehr.<sup>7,9,10</sup> The modification of the start vector  $|0\rangle$  needed to get the unprojected local density of states is described in Appendix B. The new start vector results in an improved description of the local environment of the absorbing atom compared to the method presented in Ref. 30. The elimination of rigid motions of the total cluster, translations and rotations, is very important for small cluster sizes but turned out to be insignificant for the cluster size of 749 atoms that was used here.

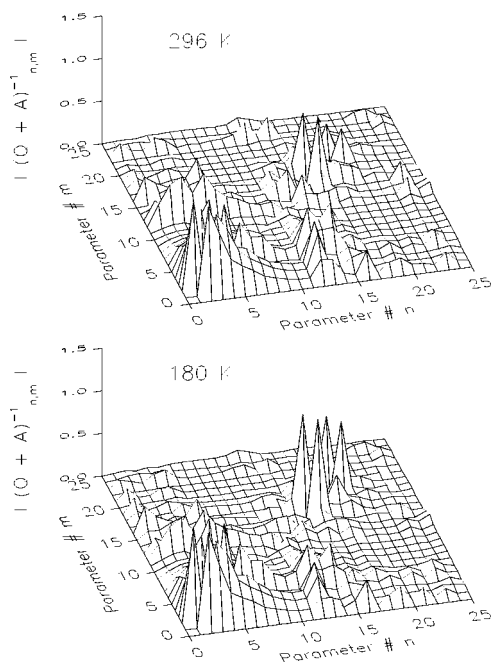


FIG. 5. Absolute values of the nondiagonal matrix elements of the *a posteriori* error-correlation matrices at  $T=180$  and  $296$  K. The parameter numbers  $n$  and  $m$  correspond to the indices of the fit-parameter vector with components  $\delta\mu_0(k_{p_1}), \dots, \delta\mu_0(k_{p_{11}}), R_1, \dots, R_{10}, \kappa_1, \kappa_2, \sigma_{\text{struct}}^2$ , and  $C_{3,1}$ .

We observe an excellent agreement between the global phonon state density of an infinite lattice and the local phonon state density of a finite cluster. It is noted that for recursion orders larger than 22 the accumulation of numerical errors leads to a loss of the orthonormality condition for the vectors generated by the Lanczos iteration. In the middle frame of Fig. 4 the unprojected VDOS deduced from the two-parameter force-field model with the *a priori* values for  $\kappa_{1,2}$  and for recursion order 16 is shown by the histogram. We observe that the two-parameter force-field model nicely reproduces the characteristic features of the VDOS extracted from inelastic neutron scattering, i.e., the sharp “optic-mode” peak<sup>31</sup> at high frequencies and a broad “acoustic-mode” peak<sup>32</sup> at moderate frequencies. The VDOS deduced from the Debye model with  $\theta_{\text{Debye}}=420$  K is represented by the solid line and shows a similar high frequency limit but no “acoustic-mode” peak. The lower frame of Fig. 4 displays the phonon state density projected onto the first scattering path and compares results of the correlated Debye model (thin solid line) and the two-parameter force-field model (histogram). Comparing the unprojected VDOS  $\rho_0(\nu)$  with the projected VDOS  $\rho_{R_1}(\nu)$  we see that  $\rho_{R_1}(\nu)$ , and thus the EXAFS Debye-Waller parameter, is less sensitive to low frequency vibrations. This is seen analytically in the Debye model, where  $\rho_0(\nu)$  vanishes as  $\nu^2$ , but  $\rho_{R_1}(\nu)$  vanishes as  $\nu^4$  when  $\nu$  approaches zero.

The rather short  $k$  range of the experimental data causes strong correlations between some of the fitting parameters and thus prevents an independent determination of these parameters. Such a behaviour is expected for the amplitudes of adjacent support points of the cubic spline function, closely

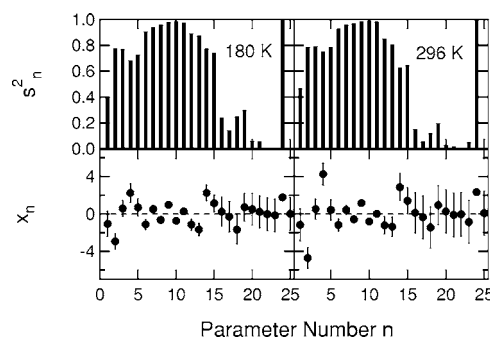


FIG. 6. The projections  $s_n^2$  into  $\mathcal{R}$  space are shown in the upper frame. In the lower frame the deviations of the model parameters from their *a priori* values are displayed together with their *a posteriori* errors. The sequence of the model parameters from left to right is  $\delta\mu_0(k_{p_1}), \dots, \delta\mu_0(k_{p_{11}}), R_1, \dots, R_{10}, \kappa_1, \kappa_2, \sigma_{\text{struct}}^2$ , and  $C_{3,1}$ .

spaced shell radii, and the two spring constants  $\kappa_1$  and  $\kappa_2$ . For both analyzed spectra the nondiagonal elements of the error-correlation matrix are shown in Fig. 5. Significant error correlations are observed between neighboring background parameters at low  $k$  values ( $n=1, \dots, 5$ ) and between closely spaced shell radii at large  $R$  ( $n=15, 16$  and  $n=18, 19$ ). The matrix also reveals minor cross correlations between background parameters and  $R_1$  ( $n=12$ ) and  $R_3$  ( $n=14$ ). The correlations between  $\kappa_1$  and  $\kappa_2$  actually are very small. These parameters essentially stay at their *a priori* values, because no changes are required by the experimental data.

The diagonal elements of the error-correlation matrix yield the *a posteriori* errors of the fit parameters. These are listed in Table I together with the *a priori* and *a posteriori* values. We observe significant deviations from the *a priori* values for the background-amplitude parameters  $\delta\mu_0(k_p)$ , for the first three shell radii  $R_1, R_2, R_3$ , and for  $\sigma_{\text{struct}}^2$ . The shifts of  $R_2$  and  $R_3$  in opposite directions change the relation  $R_3/R_2=\sqrt{2}$  of the ideal bcc structure to  $1.436\pm 0.006$  and  $1.431\pm 0.007$  at  $T=180$  and  $296$  K, respectively. The disturbance of the bcc-crystal structure is also demonstrated by the large value of  $\sigma_{\text{struct}}^2 \approx 0.007 \text{ \AA}^2$ . All deviations from the *a priori* values are represented by the dimensionless model parameters  $x_n$  which are displayed in Fig. 6. In the Bayes-Turchin data-analysis procedure the total model parameter space is divided into space  $\mathcal{R}$  where the *a posteriori* parameters are predominantly determined by the experimental data, and into space  $\mathcal{P}$  where the *a posteriori* parameters are predominantly determined by the *a priori* data (see Ref. 7). As convenient measure for the extent to which a model parameter  $x_n$  is determined by the data we use the approximate projection  $s_n^2$  of the unit vector in the direction of  $x_n$  into space  $\mathcal{R}$ .<sup>7</sup> For  $s_n^2 \approx 1$  the parameter  $x_n$  is mainly determined by the experimental data. In this case the *a posteriori* error has the usual meaning, accounting for experimental errors, uncertainties in the model, and various truncation errors of the numerical calculation. For  $s_n^2 \approx 0$   $x_n$  and its *a posteriori* error are determined by the *a priori* data. As shown in Fig. 6, many of the background-correction parameters ( $n=1, \dots, 11$ ), the lower shell radii ( $n=12, \dots, 15$ ), and the structural-disorder component ( $n=24$ ) are strongly determined by the experimental data and moved away from the *a*

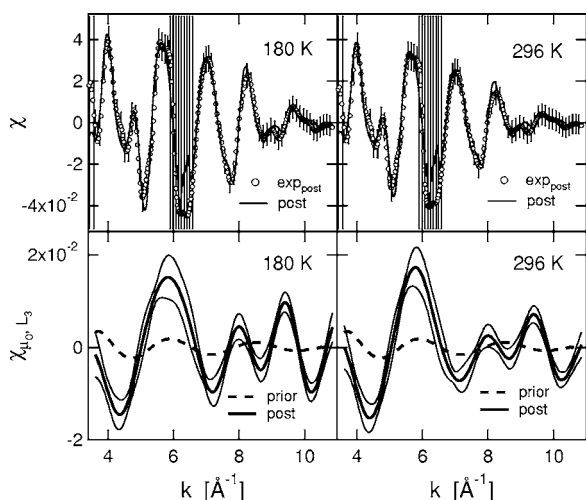


FIG. 7. Oscillations of EXAFS and the atomlike background contributions at 180 and 296 K. The upper frames display the comparison of experimental components  $\chi_{\text{exp}}$ , with error bars shown for each fourth data point, and the *a posteriori* components  $\chi_{\text{post}}$ . In the lower frames *a priori* and *a posteriori* background oscillations of the  $L_3$  components are displayed by dashed lines and thick solid lines, respectively. The one-standard deviation error band is represented by thin lines.

*priori* values. At both temperatures the third cumulant  $C_{3,1}$  of the first half path length  $R_1$  ( $n=25$ ) remains at the *a priori* value, indicating that the experimental data do not require an anharmonicity of the crystal potential.

As noted above the fitting procedure is applied to the measured absorption coefficient  $\mu_{\text{exp}}(k)$  and yields the contributions  $\chi_{L_s}(k)$  and  $\mu_{0,L_s}(k) + \delta\mu_{0,L_s}(k)$  for each edge  $L_s$  separately. In the upper frame of Fig. 7 the combined components of the EXAFS oscillations of data and model with *a posteriori* parameters are shown for  $T=180$  K and  $T=296$  K. These oscillations are defined as  $\chi(k) = [\mu(k) - \mu_0(k)] / \mu_0(k)$ , with  $\mu_0(k) = \sum_{s=1}^3 [\mu_{0,L_s}(k) + \delta\mu_{0,L_s}(k)]$ . In Fig. 7 the EXAFS oscillations  $\chi_{\text{exp}}(k)$  obtained using  $\mu_{\text{exp}}(k)$  and the *a posteriori*  $\mu_0(k)$  are called “exp<sub>post</sub>,” and the experimental errors assumed for  $\mu_{\text{exp}}(k)$  are indicated as error bars of  $\chi_{\text{exp}}(k)$ . The oscillations  $\chi_{\mu_{0,L_3}}$  of the atomlike background of the *a priori* and *a posteriori*  $L_3$  components are shown in the lower frame. Similar to the EXAFS oscillations they were defined relative to the smoothed components  $\mu_{0,L_3}(k)$  as  $\chi_{\mu_{0,L_3}} = \Delta\mu_{0,L_3}(k) / \mu_{0,L_3}(k)$  with  $\Delta\mu_{0,L_3}(k) = \mu_{0,L_3}(k) + \delta\mu_{0,L_3}(k) - \mu_{0,L_3}(k)$ . Despite the considerable differences between *a priori* and *a posteriori* background oscillations, the final background functions nearly coincide within their error bands for the two independent measurements. The enhanced oscillations have been interpreted in Ref. 6 as an atomic EXAFS process caused by backscattering of photoelectrons at interstitial charge densities between the atoms in corroboration of Ref. 1, where it was suggested that atomic EXAFS is sensitive to the nature of the bonding potential. The relatively small error bands indicate that the enhancement is well determined by the experimental data. Its amplitude is comparable to the EXAFS amplitude and underlines the importance of the atomlike background determination.

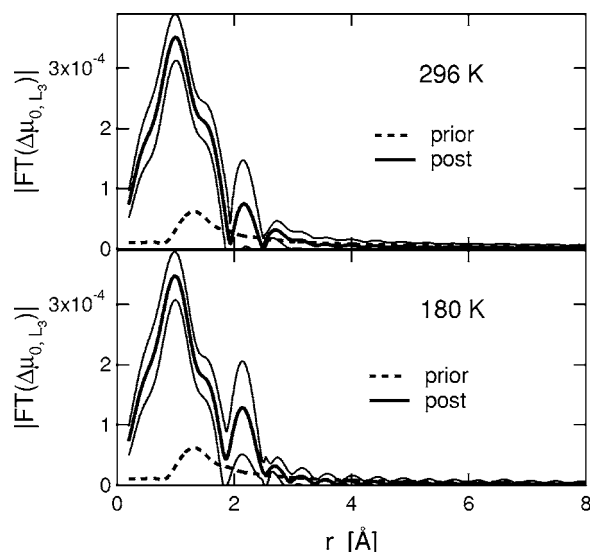


FIG. 8. Fourier transformed atomlike background oscillations of the *a priori* and *a posteriori*  $L_3$  components  $\Delta\mu_{0,L_3}$  at  $T=180$  and  $296$  K with a *a posteriori* error bands.

In the  $k$  range  $3.6 \text{ \AA}^{-1} \leq k \leq 10.6 \text{ \AA}^{-1}$  a number of  $P=11$  equally distributed support points  $k_p$  was chosen for the background correction. In this case the main frequency of the correction function is smaller than the oscillation frequency corresponding to the first scattering path length. This is demonstrated in Fig. 8, where the Fourier transformed *a priori* and *a posteriori* background oscillations are shown with *a posteriori* error bands. The frequency restriction prevents strong error correlations between  $\delta\mu_0(k_p)$  and the shell radii  $R_j$ , but it also prevents the correction of background disturbances with frequencies larger than those corresponding to  $R_1$ . We assume here that the amplitudes of these disturbances are smaller than the experimental error. Of course a perfect fit could be achieved with  $P=50$ . However, in this case the background points  $\delta\mu_0(k_p)$  dominate the fitting procedure and the  $R_j$  values stay at the *a priori* data within the *a posteriori* errors. When the correction functions are not used, i.e.,  $\delta\mu_{0,L_s}(k)=0$ , the  $\chi^2$  value of the fit is increased by a factor of 5. Relative to the best-fit case at  $T=180$  K we get moderate changes of up to  $0.018 \text{ \AA}$  for the shell radii  $R_j$ , and significant changes of  $\kappa_2$  and  $\sigma_{\text{struct}}^2$  by factors of 0.65 and 0.72, respectively. We further mention that the fitting procedure yielded different amplitudes of the background oscillation for different scattering potentials calculated by the FEFF code in the spherical muffin tin approximation.

## B. MEXAFS spectra

The XMCD signal is usually explained by a two step process. In the first step the circularly polarized photon transfers its angular momentum to the photoelectron. In case of  $2p$  core electrons the spin-orbit interaction leads to spin-polarized photoelectrons. The second step is different for the near-edge energy region and the extended energy region. At low energies the spin-polarized photoelectrons probe the density of  $m_l$  states of the  $d$  valence shell. At higher energies

the XMCD signal in magnetized materials is related to different scattering potentials for spin-up ( $\uparrow$ ,  $m_s = +1/2$ ) and spin-down ( $\downarrow$ ,  $m_s = -1/2$ ) electrons. This magnetic EXAFS effect is much smaller than the dichroism in the near-edge region, but very sensitive to the spin dependence of the excited state exchange-correlation potential. As shown by Ankudinov and Rehr in Ref. 12 for the special case of polycrystalline materials and spherical symmetry of the scattering potential, the MEXAFS fine structure  $\mu^M$ , measured by  $\mu^+$  and  $\mu^-$ , can be expressed as

$$\mu^M = \mu^+ - \mu^- = \frac{(-1)^{j-j^+} l}{(2j+1)} (\mu_{\uparrow} - \mu_{\downarrow}), \quad (11)$$

where  $\mu_{\uparrow\downarrow} = \mu_{0,\uparrow\downarrow} (1 + \chi_{\uparrow\downarrow})$  are the absorption coefficients corresponding to spin-up and spin-down electrons, respectively, and  $j^+ = l + s$ . In the following we will use this expression for our bcc-Fe sample. Within the rigid-band (RB) model the spin-dependent coefficients can be expressed as spin-averaged coefficients being shifted in energy by an exchange-related energy  $\Delta E$  (Refs. 6 and 15)

$$\mu_{\uparrow\downarrow}(E) \approx \mu_0 \left( E \pm \frac{\Delta E}{2} \right) \left[ 1 + \chi \left( E \pm \frac{\Delta E}{2} \right) \right], \quad (12)$$

where the positive sign of  $\Delta E$  is used for spin-up electrons. The MEXAFS signal of the overlapping  $L_2$  ( $j=1/2, l=1$ ) and  $L_3$  ( $j=3/2, l=1$ ) components is now approximated by

$$\begin{aligned} \mu_{L_3}^M(E) + \mu_{L_2}^M(E) &\approx \frac{1}{4} \left[ \mu_{L_3} \left( E + \frac{\Delta E}{2} \right) - \mu_{L_3} \left( E - \frac{\Delta E}{2} \right) \right] \\ &\quad - \frac{1}{2} \left[ \mu_{L_2} \left( E + \frac{\Delta E}{2} \right) - \mu_{L_2} \left( E - \frac{\Delta E}{2} \right) \right]. \end{aligned} \quad (13)$$

A relation between MEXAFS and the first derivative of EXAFS is obtained, when (a) the energy shift  $\Delta E$  is neglected in the smoothly varying central atom absorption coefficient  $\mu_0$ , (b) the difference in  $\chi$  is approximated by  $(d\chi/dE)\Delta E$ , and (c)  $\mu_{0,L_2}(E)$  is replaced by  $\mu_{0,L_3}(E)/2$ , assuming that the spin-orbit splitting  $E_{SO}$  is much smaller than the energy range over which  $\mu_{0,L_2}(E)$  changes significantly. Then the MEXAFS signal can be written as

$$\mu_{L_3}^M(E) + \mu_{L_2}^M(E) \approx \frac{\mu_{0,L_3}(E)}{4} \left[ \frac{d\chi_{L_3}(E)}{dE} - \frac{d\chi_{L_2}(E)}{dE} \right] \Delta E \quad (14)$$

$$\approx E_{SO} \frac{\mu_{0,L_3}(E)}{4} \left[ \frac{d^2\chi_{L_3}(E - E_{SO}/2)}{dE^2} \right] \Delta E, \quad (15)$$

where in Eq. (15)  $\chi_{L_2}(E)$  has been replaced by  $\chi_{L_3}(E - E_{SO})$ . Within these approximations the energy dependence of MEXAFS is described by the energy dependence of EXAFS and the spin dependence is expressed by the exchange-related energy  $\Delta E$  and the spin-orbit splitting  $E_{SO}$ .

In Fig. 9 the approximations (13) and (15) are verified by FEFF computations for Fe at  $T=0$  assuming perfect ordering of spins. The HL energy density functional has been used

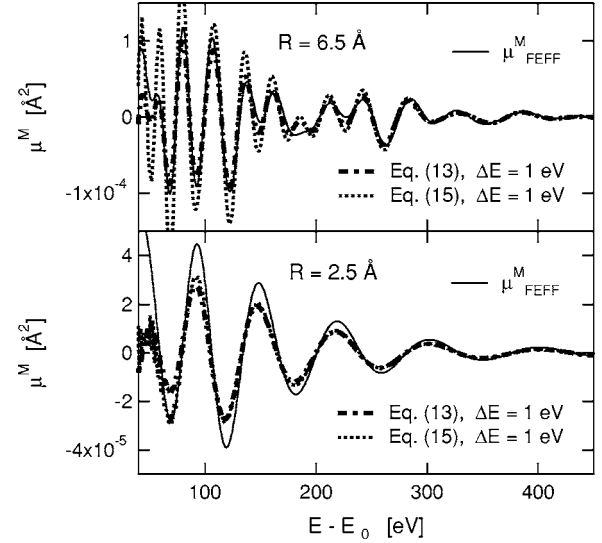


FIG. 9. MEXAFS oscillations  $\mu^M$  (solid lines) computed by FEFF are compared with the approximations of Eqs. (13) and (15) of Sec. III B. In the upper frame results are shown for a cluster with radius  $R=6.5$  Å, and in the lower frame the computations have been performed for a cluster with radius  $R=2.5$  Å.

and the spin magnetic moment of each atom was set to 2.2 Bohr magnetons. In the lower frame the results of the model calculations are displayed for the first shell of an iron cluster and in the upper frame the model calculations were performed for a cluster with radius  $R=6.5$  Å. In both frames the MEXAFS oscillations are shown by the solid line, the RB model approximation [Eq. (13)] by the dash-dotted line, and the second-derivative approximation [Eq. (15)] by the dotted line. The differences between the curves representing the results of Eqs (13) and (14) are tiny. Thus the MEXAFS signal computed from Eq. (14) is not shown. For all approximations the exchange energy  $\Delta E$  was set to  $\Delta E=1$  eV. We observe fair agreement at lower energies and good agreement at higher energies. Comparing the curves of both frames we conclude that in the upper frame the component of the first shell is small compared to the higher shell components. This effect was already observed by Wende *et al.*<sup>6,33</sup> It is noted that the sign of  $\Delta E$  used here is consistent with FEFF results but different from the one used by Wende *et al.*

In Figs. 10 the experimental MEXAFS signals  $\mu_{\text{exp}}^M$  measured at  $T=180$  and  $296$  K are compared with the RB model approximations of Eqs. (13) and (15). The components  $\chi_{L_2}$  and  $\chi_{L_3}$  have been obtained from the fit to the corresponding measured absorption coefficient  $\mu_{\text{exp}}$  as described in Sec. III A. The energy dependence of the measured signal is reproduced very well with  $\Delta E=-1$  eV, i.e., just the opposite sign compared to the results from the HL energy density functional. The change of sign for  $\Delta E$  occurs roughly 50 eV behind the  $L_3$ -edge. This is shown in Fig. 11. Here we compared  $\mu_{\text{exp}}^M$  and  $\mu_{\text{FEFF}}^M$  in the energy range  $705 \text{ eV} \leq E \leq 785 \text{ eV}$ . Please note that the scale of  $\mu^M$  was changed by a factor of 100 for energies  $E \geq 740 \text{ eV}$ . The FEFF calculations displayed by the solid line were obtained using the options for full multiple scattering, automated self-consistent potential calculations and the HL energy density functional.



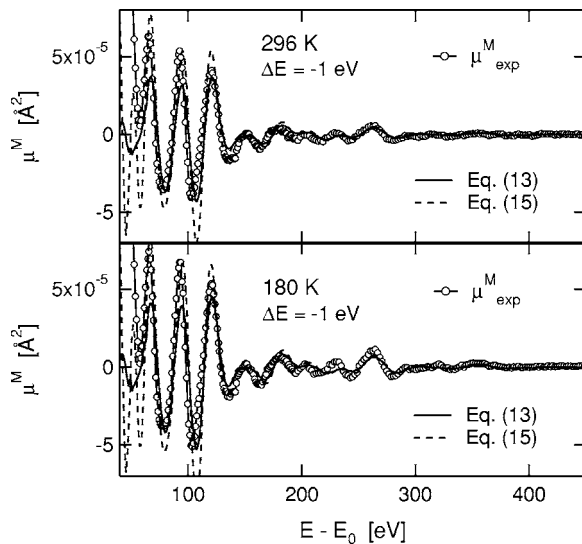


FIG. 10. MEXAFS oscillations  $\mu_{\text{exp}}^M$  (open circles) measured at temperatures  $T=180$  K and  $T=296$  K are compared with the approximations given in Eq. (13) (solid lines) and Eq. (15) (dashed lines) of Sec. III B.

Whereas the signs of measured and computed XMCD spectra coincide in the edge region, we observe a sign change above the edge region between 760 and 780 eV. The discrepancies of the white line intensities are caused by experimental and model uncertainties as well. The dotted line in Fig. 11 represents the FEFF calculation where the HL energy density functional was replaced by the spin and energy dependent Dirac-Hara exchange-correlation potential combined with the imaginary part of the HL functional.<sup>12</sup> This interaction potential obviously yields a better description of the MEXAFS oscillations. Comparison of both FEFF results in the extended energy regime demonstrates the sensitivity of the MEXAFS signal to the spin dependence of the interaction potential. MEXAFS is a very specific probe for the fine tuning of the exchange-correlation potential. Whereas in many applications the HL energy density functional has proved to be the best choice to model the EXAFS signal, it fails to describe magnetic EXAFS for iron.

#### IV. CONCLUSIONS

EXAFS oscillations contain informations about the local crystallographic structure and lattice dynamics. Great care is necessary to identify these oscillations from the measured absorption coefficient. Applying our Bayes-Turchin data analysis procedure we demonstrated that the simultaneous treatment of background and structure parameters can be performed reliably. Thus, the determination of the atomlike background component of the absorption coefficient provides a useful probe of the bonding potential and of chemical effects. The present analysis confirms the atomic EXAFS oscillations observed by Wende *et al.*<sup>6</sup> However, we note that the number of background spline points were restricted to

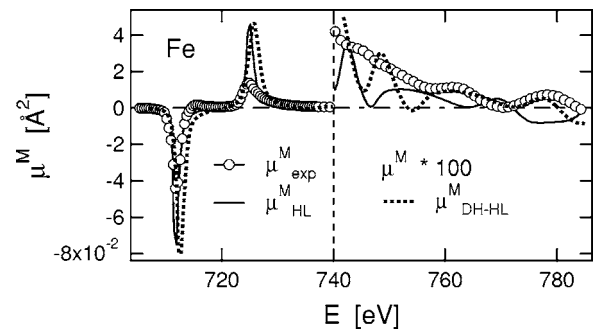


FIG. 11. The MEXAFS signal  $\mu_{\text{exp}}^M$  (open circles) measured at  $T=180$  K is compared with FEFF calculations for  $T=0$  K. FEFF results using the HL exchange-correlation potential are displayed by the solid line and results obtained by the DH-HL exchange-correlation potential are shown by the dotted line. Experimental data points and FEFF results were multiplied by a factor of 100 at energies  $E \geq 740$  eV.

$P=11$  to avoid large error correlations between background and structure parameters. For  $P > 11$  the frequencies of the background oscillations enter the frequency region of the EXAFS oscillations. It was assumed that the experimental uncertainty of  $\mu_{\text{exp}}$  is larger than the amplitudes of high frequency background disturbances.

We observe a slight distortion of the crystallographic bcc structure of the Fe film grown on bcc-V. This distortion shows up in the shifts of the first three shell radii and a significant structural disorder. Because the reference energy  $E_0$  had been fixed only relative shifts of  $R_j$  are relevant. The shifts of  $R_2$  and  $R_3$  in opposite directions indicate that the relation  $R_3 = \sqrt{2}R_2$  of the ideal bcc structure is broken. The shifts are the same within the *a posteriori* errors for the two independent measurements. For the structural disorder we obtain a slightly smaller value at lower temperature. The determination of the nature of this distortion and the separation between surface and bulk effects cannot be accomplished by our measurements.

Due to the small  $k$  range of the measurements the information of the experimental data was not sufficient to extract lattice dynamics information unambiguously. Additional information was taken from inelastic neutron scattering. Using BvK parameters and the recursion method of Poiarkova and Rehr with modified start vector, we calculated the unprojected local VDOS. Comparison with the phonon state density extracted from phonon dispersion relations indicates that the recursion method used to calculate the local VDOS of a finite cluster can be applied reliably. We further showed that the dynamical matrix of the force-field model can be equally described by two spring constants. This is a promising method for inhomogeneous and amorphous materials.

An iron cluster with radius  $R=8 \text{ \AA}$  and 97 scattering paths was used in the EXAFS analysis. Long scattering paths are needed to describe the fine structure in EXAFS and MEXAFS at small  $k$  values. Different from the magnetic signal in the near-edge region the MEXAFS signal is largely independent of state density differences for spin-up and spin-down electrons in the valence band and represents a very sensitive and specific probe of the spin dependence of

excited-state exchange-correlation potentials. Contrary to the predictions of the HL energy density functional in combination with the rigid-band model the energy dependence of the measured MEXAFS oscillations can be described by a negative exchange-related energy.

### APPENDIX A: CALCULATION OF THE “PENALTY” A PRIORI PROBABILITY

It is required that the energy integral of the correction spline function is zero:

$$I = \int \delta\mu_0(E) dE = \int_{k_1}^{k_p} \delta\mu_0(k) k dk = 0. \quad (\text{A1})$$

The dimensionless model parameters  $x_p$  ( $p=1, \dots, P$ ) that correspond to the amplitudes  $\delta\mu_0(k_p)$  at the support points  $k_p$  constitute the components of the vector  $\tilde{\mathbf{x}}$  which is part of the model parameter vector  $\mathbf{x}$  (see Ref. 7). Partitions  $I(x_p)$  are defined by

$$I(x_p) = \int_{k_{p-1}}^{k_p} \delta\mu_0(k) k dk \quad (\text{A2})$$

that sum up to  $I$ . At iteration step  $\nu$  the integral  $I(\tilde{\mathbf{x}})$  is expanded around  $\tilde{\mathbf{x}}^{(\nu)}$ :

$$I(\tilde{\mathbf{x}}) = I(\tilde{\mathbf{x}}^{(\nu)}) + \sum_n \frac{\partial I(\tilde{\mathbf{x}}^{(\nu)})}{\partial x_n^{(\nu)}} (x_n^{(\nu+1)} - x_n^{(\nu)}). \quad (\text{A3})$$

We call the partial derivatives  $\tilde{G}_n^{(\nu)}$ . They are zero if the fit parameter  $x_n$  does not correspond to an amplitude  $\delta\mu_0(k_p)$ . Now a “penalty” *a priori* probability  $P_{\text{pen}}$  is introduced as Gaussian:

$$P_{\text{pen}} \sim e^{-\chi_{\text{pen}}^2/2} \quad (\text{A4})$$

with

$$\chi_{\text{pen}}^2 = I(\tilde{\mathbf{x}}) q I(\tilde{\mathbf{x}}) \quad (\text{A5})$$

$$= (\mathbf{x}^{(\nu+1)} - \mathbf{x}^{(\nu)})^T \tilde{\mathbf{G}}^{T(\nu)} q \tilde{\mathbf{G}}^{(\nu)} (\mathbf{x}^{(\nu+1)} - \mathbf{x}^{(\nu)}) - 2\tilde{\mathbf{b}}^T (\mathbf{x}^{(\nu+1)} - \mathbf{x}^{(\nu)}) + \text{const} \quad (\text{A6})$$

and

$$\tilde{\mathbf{Q}}^{(\nu)} = \tilde{\mathbf{G}}^{T(\nu)} q \tilde{\mathbf{G}}^{(\nu)}, \quad \tilde{\mathbf{b}}^{(\nu)} = -I(\tilde{\mathbf{x}}^{(\nu)}) q \tilde{\mathbf{G}}^{(\nu)}, \quad (\text{A7})$$

where  $q$  is set to a sufficiently large number. We have used  $q$  equal to the largest eigenvalue of the information matrix  $\mathbf{Q}$ . The “penalty” condition is introduced into the iteration procedure described in Ref. 7 substituting the information matrix  $\mathbf{Q}^{(\nu)}$  by  $\mathbf{Q}^{(\nu)} + \tilde{\mathbf{Q}}^{(\nu)}$  and the inhomogeneous term  $\mathbf{b}^{(\nu)}$  by  $\mathbf{b}^{(\nu)} + \tilde{\mathbf{b}}^{(\nu)}$ .

### APPENDIX B: RECURSION RELATION FOR THE UNPROJECTED VDOS

In a cluster of  $N$  atoms the projected Debye-Waller factor for the scattering path  $j$  can be written in terms of the projected VDOS  $\rho_j(\omega)$

$$\sigma_j^2 = \frac{\hbar}{2\mu_j} \int_0^\infty \omega^{-1} \coth(\beta\hbar\omega/2) \rho_j(\omega) d\omega, \quad (\text{B1})$$

where the projected VDOS is given by<sup>9,10</sup>

$$\begin{aligned} \rho_j(\omega) d\omega &= \sum_\gamma |\langle j | \gamma \rangle|^2 \delta(\omega - \omega_\gamma) d\omega \\ &= -\frac{1}{\pi} \text{Im} \langle j | \frac{1}{z - \Phi + i\epsilon} | j \rangle dz. \end{aligned} \quad (\text{B2})$$

Here  $\Phi$  is the  $3N$ -dimensional dynamical matrix,  $|\gamma\rangle$  and  $\omega_\gamma^2$  are its eigenvectors and eigenvalues, respectively, and  $z = \omega^2$ . If vectors in the  $3N$ -dimensional space of displacements are labeled by  $n, \alpha$ , where  $n=1, \dots, N$  and  $\alpha=1, 2, 3$ , the components of the normalized vector  $|j\rangle$  are given by  $(1/2)\sqrt{\mu_j/M}(\hat{r}_{n_i, n_{i-1}}^\alpha + \hat{r}_{n_i, n_{i+1}}^\alpha)$  if  $n$  equals one of the  $N_j$  nodes  $n_i$  of the scattering path  $j$  and are zero otherwise. The  $\hat{r}_{n_i, n_j}^\alpha$  are the Cartesian components of the unit vector in the direction from lattice point  $n_i$  to lattice point  $n_j$  and the mass  $\mu_j$  is defined by  $M/\mu_j = \sum_{i=1}^{N_j} \sum_{\alpha=1}^3 (\hat{r}_{n_i, n_{i-1}}^\alpha + \hat{r}_{n_i, n_{i+1}}^\alpha)^2/4$ . It was shown in Refs. 7, 9, and 10 that the Lanczos algorithm can be used to generate a Krylov space by means of the dynamical matrix  $\Phi$  and the start vector  $|j\rangle$ , to obtain a continued fraction representation of the Green’s function  $\langle j | (z - \Phi + i\epsilon)^{-1} | j \rangle$  on the right-hand side of Eq. (B2) and an approximation to the integral in Eq. (B1) by a Gaussian sum to the weight function  $\rho_j(\omega)$ .

Analogously the unprojected Debye-Waller parameter is given in terms of the unprojected VDOS  $\rho_0(\omega)$

$$\sigma^2 = \frac{\hbar}{2M} \int_0^\infty \omega^{-1} \coth(\beta\hbar\omega/2) \rho_0(\omega) d\omega, \quad (\text{B3})$$

$\rho_0(\omega)$  being defined by

$$\rho_0(\omega) d\omega = \sum_\gamma \delta(\omega - \omega_\gamma) d\omega = -\frac{1}{\pi} \text{Im} \text{tr} \left( \frac{1}{z - \Phi + i\epsilon} \right) dz. \quad (\text{B4})$$

We shall now show that the trace can be expressed by a Green’s function as in Eq. (B2) with an appropriately chosen initial vector  $|0\rangle$ , thus allowing the use of the efficient Lanczos algorithm and the representation of the integral in Eq. (B3) by a Gaussian sum.

We define a complete set of orthonormal vectors  $|n\alpha\rangle$  with components 1 at site  $n$ , direction  $\alpha$ , all other components 0. For periodic boundary conditions the eigenstates  $|\gamma\rangle$  may be represented by  $|\gamma\rangle = N^{-1/2} \hat{\epsilon}(\mathbf{k}, \alpha') \exp(i\mathbf{k} \cdot \mathbf{R}_n)$ , with the crystal momentum  $\mathbf{k}$  in the Brillouin zone. Then

$$\begin{aligned} \text{tr}\left(\frac{1}{z-\Phi+i\epsilon}\right) &= \sum_{n,\alpha} \left\langle n\alpha \left| \frac{1}{z-\Phi+i\epsilon} \right| n\alpha \right\rangle \\ &= \sum_{n,\alpha;\mathbf{k},\alpha'} |\langle n\alpha | \hat{\epsilon}(\mathbf{k}, \alpha') \rangle|^2 \frac{1}{z-\omega_\alpha^2+i\epsilon}. \end{aligned} \quad (\text{B5})$$

We have  $\langle n\alpha | \hat{\epsilon}(\mathbf{k}, \alpha') \rangle \propto \delta_{\alpha,\alpha'}$  and

$$\begin{aligned} \sum_{\alpha=1}^3 |\langle n\alpha | \hat{\epsilon}(\mathbf{k}, \alpha) \rangle|^2 &= (1/N) \{ [\hat{\epsilon}(\mathbf{k}, x)\hat{x}]^2 + [\hat{\epsilon}(\mathbf{k}, y)\hat{y}]^2 \\ &\quad + [\hat{\epsilon}(\mathbf{k}, z)\hat{z}]^2 \} = (1/N), \end{aligned} \quad (\text{B6})$$

independent of  $n$ . For a cubic lattice the contribution of each of the three terms to the sum should be the same for symmetry reasons. With the choice  $|0\rangle = |1, 0, \dots\rangle$  we therefore get

$$\text{tr}\left(\frac{1}{z-\Phi+i\epsilon}\right) = 3 \left\langle 0 \left| \frac{1}{z-\Phi+i\epsilon} \right| 0 \right\rangle. \quad (\text{B7})$$

Substitution of this result into Eq. (B4) brings it to the desired form of Eq. (B2). For less symmetric lattices one would have to repeat this procedure for all nonequivalent atoms and add the results with appropriate weights.

A cluster of  $N$  atoms, cut out of the lattice, feels no restoring forces against rigid translations and rotations. The corresponding modes have therefore vanishing eigenvalues. These spurious features of the VDOS of a free cluster are particularly unwanted since the factor  $\omega^{-1} \coth(\beta\omega/2)$  multiplying  $\rho_j(\omega)$  in the integrand of Eq. (B1) has a second order pole at  $\omega=0$ .

The influence of the rigid motions on the VDOS can be eliminated in the following way. When the start vector  $|0\rangle$  of the Lanczos algorithm lies completely in a space spanned by only a subset of the eigenvectors of the dynamical matrix  $\Phi$ , the Lanczos iteration does not lead out of this space (except for rounding errors). One has therefore only to subtract from  $|0\rangle$  any component belonging to the space spanned by the displacement vectors of the three translations

$$|a_x\rangle = N^{-1/2} |100; 100; \dots 100\rangle \quad (\text{B8})$$

and analogously  $|a_y\rangle$  and  $|a_z\rangle$  and the three rigid rotations around the  $x$ ,  $y$ , and  $z$  axis. The corresponding displacement fields can be generated from the vectors  $\mathbf{R}_n$  by the orthogonal matrices

$$\begin{aligned} D_x &= \begin{pmatrix} 1 & 0 & 0 \\ 0 & 0 & -1 \\ 0 & 1 & 0 \end{pmatrix}, & D_y &= \begin{pmatrix} 0 & 0 & 1 \\ 0 & 1 & 0 \\ -1 & 0 & 0 \end{pmatrix}, \\ D_z &= \begin{pmatrix} 0 & -1 & 0 \\ 1 & 0 & 0 \\ 0 & 0 & 1 \end{pmatrix}, \end{aligned} \quad (\text{B9})$$

with  $\det(D_\alpha) = +1$  for  $\alpha = x, y, z$ . The normalized displacement vectors corresponding to the three rotations are

$$|d_\alpha\rangle = \left( \sum_{n=1}^N R_n^2 \right)^{-1/2} |000; D_\alpha \mathbf{R}_2; \dots D_\alpha \mathbf{R}_N\rangle, \quad (\text{B10})$$

$\alpha = x, y, z$ . Note that these vectors depend only on the lattice type and the cluster size, not on the lattice constant.

Since  $|1\ 0\ 0; 0\ 0\ 0\dots\rangle$  is already orthogonal to all rigid displacement fields, except  $|a_x\rangle$ , the properly projected and normalized start vector for the Lanczos iteration is up to errors of order  $1/N^2$

$$|0\rangle_{\text{proj}} = \frac{1}{\sqrt{N(N-1)}} |N-100; -100; \dots -100\rangle. \quad (\text{B11})$$

The start vector  $|0\rangle$  for the projected Debye-Waller parameter has in general to be corrected for all six spurious modes. It is convenient to use the Gram-Schmidt orthogonalization procedure to generate an orthonormal basis  $|c_j\rangle$ ,  $j=1, \dots, 6$ , in this six dimensional space. Denoting

$$\begin{aligned} |c_1\rangle &= |a_x\rangle, & |c_2\rangle &= |a_y\rangle, & |c_3\rangle &= |a_z\rangle, & |d_4\rangle &= |d_x\rangle, \\ |d_5\rangle &= |d_y\rangle, & |d_6\rangle &= |d_z\rangle, \end{aligned} \quad (\text{B12})$$

one obtains recursively

$$|c_j\rangle = N_j \left( |d_j\rangle - \sum_{i=1}^{j-1} \langle c_i | d_j \rangle |c_i\rangle \right), \quad j=4, 5, 6, \quad (\text{B13})$$

where the normalization constant is given by

$$N_j^{-2} = 1 - \sum_{i=1}^{j-1} \langle c_i | d_j \rangle^2. \quad (\text{B14})$$

The normalized, projected start vector is then

$$|0\rangle_{\text{proj}} = \left[ 1 - \sum_{i=1}^6 \langle c_i | 0 \rangle^2 \right]^{-1/2} \left( |0\rangle - \sum_{i=1}^6 \langle c_i | 0 \rangle |c_i\rangle \right). \quad (\text{B15})$$

<sup>1</sup>J. J. Rehr and R. C. Albers, Rev. Mod. Phys. **72**, 621 (2000).

<sup>2</sup>A. Di Cicco, Phys. Rev. B **53**, 6174 (1996).

<sup>3</sup>H. J. Krappe and H. H. Rossner, Phys. Rev. B **70**, 104102 (2004).

<sup>4</sup>A. Filippini and A. Di Cicco, Phys. Rev. A **52**, 1072 (1995).

<sup>5</sup>J. J. Rehr, C. H. Booth, F. Bridges, and S. I. Zabinsky, Phys. Rev. B **49**, 12347 (1994).

<sup>6</sup>H. Wende, Rep. Prog. Phys. **67**, 2105 (2004).

<sup>7</sup>H. J. Krappe and H. H. Rossner, Phys. Rev. B **66**, 184303 (2002).

<sup>8</sup>A. L. Ankudinov, B. Ravel, J. J. Rehr, and S. D. Conradson, Phys. Rev. B **58**, 7565 (1998); A. L. Ankudinov, Ph.D. thesis, University of Washington, 1996.

<sup>9</sup>A. V. Poiarkova and J. J. Rehr, Phys. Rev. B **59**, 948 (1999).

- <sup>10</sup>A. V. Poiarkova and J. J. Rehr, *J. Synchrotron Radiat.* **6**, 313 (1999).
- <sup>11</sup>G. Schütz, W. Wagner, W. Wilhelm, P. Kienle, R. Zeller, R. Frahm, and G. Materlik, *Phys. Rev. Lett.* **58**, 737 (1987).
- <sup>12</sup>A. Ankudinov and J. J. Rehr, *Phys. Rev. B* **52**, 10214 (1995).
- <sup>13</sup>A. L. Ankudinov and J. J. Rehr, *Phys. Rev. B* **56**, R1712 (1997).
- <sup>14</sup>G. Schütz and D. Ahlers, in *Spin-Orbit-Influenced Spectroscopies of Magnetic Solids*, edited by H. Ebert and G. Schütz, Vol. 466 of *Lecture Notes in Physics* (Springer, Berlin, 1996), p. 229.
- <sup>15</sup>C. Brouder, M. Alouani, C. Giorgetti, E. Dartyge, and F. Baudelet, in *Spin-Orbit-Influenced Spectroscopies of Magnetic Solids* (Ref. 14), p. 259.
- <sup>16</sup>H. Ebert, V. Popescu, D. Ahlers, G. Schütz, L. Lemke, H. Wende, P. Srivastava, and K. Baberschke, *Europhys. Lett.* **42**, 295 (1998).
- <sup>17</sup>M. Wuttig and X. Liu, Vol. 206 of *Springer Tracts in Modern Physics*, edited by G. Höhler (Springer, Berlin, 2004).
- <sup>18</sup>R. W. G. Wyckoff, *Crystal Structures* (Wiley, New York, 1963), Vol. 1.
- <sup>19</sup>T. Nawrath, H. Fritzsche, and H. Maletta, *Surf. Sci.* **414**, 209 (1998).
- <sup>20</sup>T. Nawrath, H. Fritzsche, F. Klose, J. Nowikow, and H. Maletta, *Phys. Rev. B* **60**, 9525 (1999).
- <sup>21</sup>D. Schmitz, J. Hauschild, P. Imperia, Y. T. Liu, and H. Maletta, *J. Magn. Magn. Mater.* **269**, 89 (2004).
- <sup>22</sup>U. Englisch, H. Rossner, H. Maletta, J. Bahrtdt, S. Sasaki, F. Senf, K. J. S. Sawhney, and W. Gudat, *Nucl. Instrum. Methods Phys. Res. A* **467-468**, 541 (2001).
- <sup>23</sup>A. Rogalev, V. Gotte, J. Goulon, Ch. Gauthier, J. Chavanne, and P. Elleaume, *J. Synchrotron Radiat.* **5**, 989 (1998).
- <sup>24</sup>L. Hedin and S. Lundqvist, *Solid State Phys.* **23**, 1 (1969).
- <sup>25</sup>R. Nakajima, J. Stöhr, and Y. U. Idzerda, *Phys. Rev. B* **59**, 6421 (1999).
- <sup>26</sup>P. Fornasini, S. a Beccara, G. Dalba, R. Grisenti, A. Sanson, M. Vaccari, and F. Rocca, *Phys. Rev. B* **70**, 174301 (2004).
- <sup>27</sup>D. E. Sayers, E. A. Stern, and F. W. Lytle, *Phys. Rev. Lett.* **27**, 1204 (1971).
- <sup>28</sup>V. J. Minkiewicz, G. Shirane, and R. Nathans, *Phys. Rev.* **162**, 528 (1967).
- <sup>29</sup>P. H. Dederichs, H. Schober, and D. J. Sellmyer, *Landolt-Börnstein: Numerical Data and Functional Relationships in Science and Technology*, edited by K.-H. Hellwege and J. L. Olsen (Springer, Berlin, 1981), Vol. 13a.
- <sup>30</sup>H. H. Rossner, E. Holub-Krappe, M. Fieber-Erdmann, and H. J. Krappe, *Phys. Scr.* **T115**, 45 (2005).
- <sup>31</sup>Vibrational modes where neighboring atoms move predominately against each other.
- <sup>32</sup>Vibrational modes where neighboring atoms move almost in phase.
- <sup>33</sup>H. Wende, P. Srivastava, D. Arvanitis, F. Wilhelm, L. Lemke, A. Ankudinov, J. J. Rehr, J. W. Freeland, Y. U. Idzerda, and K. Baberschke, *J. Synchrotron Radiat.* **6**, 696 (1999).